IOPscience iopscience.iop.org

Home Search Collections Journals About Contact us My IOPscience

In situ neutron diffraction study of micromechanical interactions and phase transformation in Ni–Mn–Ga alloy under uniaxial and hydrostatic stress

This article has been downloaded from IOPscience. Please scroll down to see the full text article.

2008 J. Phys.: Condens. Matter 20 104256

(http://iopscience.iop.org/0953-8984/20/10/104256)

View the table of contents for this issue, or go to the journal homepage for more

Download details:
IP Address: 129.252.86.83
The article was downloaded on 29/05/2010 at 10:44

Please note that terms and conditions apply.

J. Phys.: Condens. Matter **20** (2008) 104256 (6pp) doi:10.1088/0953-8984/20/10/104256

In situ neutron diffraction study of micromechanical interactions and phase transformation in Ni–Mn–Ga alloy under uniaxial and hydrostatic stress

R Lin Peng[1], Y D Wang[2], Z H Nie[2], E C Oliver[3], S Johansson[1], Y D Liu[2], Y Ren[4], J D Jorgensen[5] and J Fieramosca[5]

[1] Department of Management and Engineering, Linköping University, S-58183 Linköping, Sweden
[2] Key Laboratory for Anisotropy and Texture of Materials (Ministry of Education), Northeastern University, Shenyang 110004, People's Republic of China
[3] ISIS Facility, CCLRC Rutherford Appleton Laboratory, Chilton, Didcot OX11 0QX, UK
[4] X-ray Science Division, Argonne National Laboratory, IL 60439, USA
[5] Intense Pulsed Neutron Source, Argonne National Laboratory, IL 60439, USA

Received 16 July 2007, in final form 28 August 2007
Published 19 February 2008
Online at stacks.iop.org/JPhysCM/20/104256

Abstract
This paper deals with the experimental study of stress-induced phase transformation in a polycrystalline Ni–Mn–Ga alloy under uniaxial compression and its powder under hydrostatic compression. *In situ* neutron diffraction experiments were employed to follow changes in the structure and lattice strains caused by the applied stresses. Large lattice strains that are dependent on the lattice planes or grain orientations were observed in the parent Heusler phase for both the bulk material and the powder sample. The development of such anisotropic strains and the influence of external load conditions are discussed in the paper.

(Some figures in this article are in colour only in the electronic version)

1. Introduction

The 'shape memory effect' (SME) is a unique property of certain alloys exhibiting a diffusionless structural change through which a high temperature parent phase (austenite) is converted to a low temperature phase (martensite). Such shape memory alloys (SMAs), after being deformed in the martensitic state, can restore their original shape upon the reversal transformation that can be induced by external thermal or magnetic fields. When loaded in the austenitic state, SMAs can exhibit another type of shape memory effect which is called pseudoelasticity. In this case, a large reversible deformation is generated by a stress-induced martensitic transformation, which can be recovered through the reverse transformation upon unloading or annealing. Materials with SME have been used as functional materials in pipeline couplings, antennae for cellular phones, medical implants, and various actuators and sensors. Recently, alloys based on the Ni–Mn–Ga system have emerged as a new class of SMAs superior to the classic SMAs because of their larger strain and faster response to magnetic fields. Since the magnetic-field-induced strain was reported in a Ni_2MnGa single crystal by Ullakko *et al* [1], the potential technological significance of the Ni–Mn–Ga system has stimulated considerable research interests which have focused on understanding the phase transformation behaviour and the mechanism behind the shape memory effect [1–5]. The high temperature phase of the alloys often called the Heusler phase is recognized to be an ordered $L2_1$ crystal structure. Upon cooling a martensitic phase of lower symmetry occurs through a diffusionless, displacive structural change. Depending on the chemical composition and transformation temperature, three martensitic structures, namely tetragonal non-modulated and orthorhombic modulated five-layered or seven-layered martensite, are commonly found in the Ni–Mn–Ga alloys. Such crystallographic structures can also be obtained through stress-induced transformation [6].

So far investigations on stress-induced martensitic transformation processes and the associated pseudoelasticity

 © 2008 IOP Publishing Ltd Printed in the UK

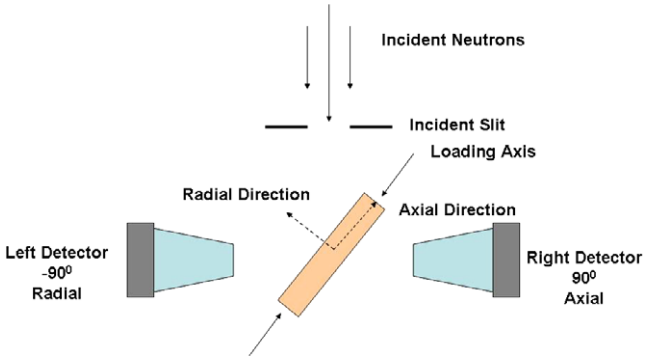

Figure 1. Schematic of the *in situ* experiment on ENGIN-X.

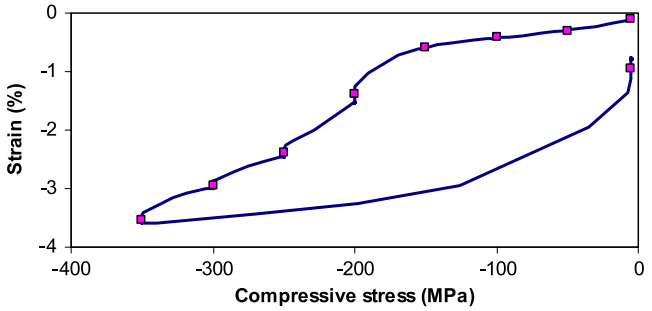

Figure 2. Macroscopic stress–strain curve recorded during the *in situ* experiment. The symbols indicate the stress levels at which the load was held constant while neutron diffraction spectra were collected.

have largely focused on single crystals. From the point of view of engineering applications, polycrystalline SMAs are equally interesting. The existence of grain boundaries provides mechanisms for controlling the mechanical properties, which are important for certain engineering applications of shape memory alloys. Due to the grains boundaries and grain orientation distributions, phase transformation is a more complicated process. In addition, interactions between the phase transformation strains and the microstructural features can lead to large intergranular stresses which can affect the continued transformation. It was reported that internal stresses from sample preparation can assist martensitic transformation [7]. Recently, the import role of internal stresses in SME was also suggested [8] and the memory of the intergranular stress during thermoelastic transformation was demonstrated [9].

The purpose of the current work is to investigate the stress-induced phase transformation process and the accompanied development of internal stresses/strains in a polycrystalline $Ni_{48}Mn_{30}Ga_{22}$ alloy using the *in situ* neutron diffraction technique. In the paper, the microscopic behaviour of the parent austenitic phase under uniaxial compression and hydrostatic pressure, respectively, is explored by analyzing neutron diffraction spectra recorded during the *in situ* experiments.

2. Experimental details

2.1. Materials

The $Ni_{48}Mn_{30}Ga_{22}$ alloy used in this study is a 10 mm diameter ingot which was obtained through direct casting of the arc-melted metal in an ice-water cooled copper mold [10]. By spark erosion cutting, a cylindrical specimen of 7 mm in diameter and 20 mm in length was taken from the ingot for the neutron diffraction experiment under *in situ* compression. Some of the material was crushed into powder, which was then used for the neutron diffraction experiment under hydrostatic pressure.

The crystal structure and the thermoelastic phase transformation of the alloy were studied by neutron diffraction in [10]. The crystallographic structure of the material at ambient temperature was determined to be a $L2_1$ ordered structure with $a = b = c = 5.8398$ Å that belongs to the space group $Fm\bar{3}m$. Upon cooling in stress-free condition, the alloy transforms to martensite at 269 K and reaches a fully martensitic state at 260 K. By neutron diffraction experiments, the crystallographic structure is identified as seven-layered martensite with orthorhombic unit cell in the space group $pnnm$. The crystallographic correspondence between the phases, as reported by Brown *et al* [5], are: $[100]_{LP} \parallel [1\bar{1}0]_{HP}$, $[010]_{LP} \parallel [110]_{HP}$ and $[001]_{LP} \parallel [001]_{HP}$. The suffixes HP and LP are used in this paper to denote the Heusler and martensitic phase, respectively. The lattice parameters are: $a = 4.2309$ Å, $b = 29.4066$ Å, and $c = 5.5664$ Å. Reverse transformation from martensite to austenite at heating occurs in the temperature range of 275–286 K. No intermartensitic transformation was observed.

2.2. In situ neutron diffraction experiments and data reduction

The neutron diffraction experiment under *in situ* compression was carried out using the time-of-flight (TOF) neutron diffractometer ENGIN-X at the ISIS facility of Rutherford Appleton Laboratory in the UK. A schematic of the experimental set-up is shown in figure 1. The sample axis was aligned horizontally at 45° to the incident beam, such that the right and left detectors collected the axial and the transverse spectrum, respectively. The neutron gauge volume, which was centred at the specimen axis, was 4 mm in the scattering plane and 7 mm out of the scattering plane. Via a test rig, the specimen was axially compressed at ambient temperature. The applied compressive stress was increased stepwise from −5 MPa, a small load to hold the specimen in the test rig, to −350 MPa, the peak stress of this experiment. Unloading from the peak stress to −5 MPa occurred in one step. The macroscopic stress–strain curve recorded during the *in situ* experiment is plotted in figure 2, with the squares indicating stress levels at which the load was held constant for the recording of neutron TOF spectra. The holding time was 15 min for the fully austenitic state and 45 min at the martensitic transformation stage. For loading above −150 MPa and unloading at −5 MPa, obvious creep (deformation) was observed during the holding time.

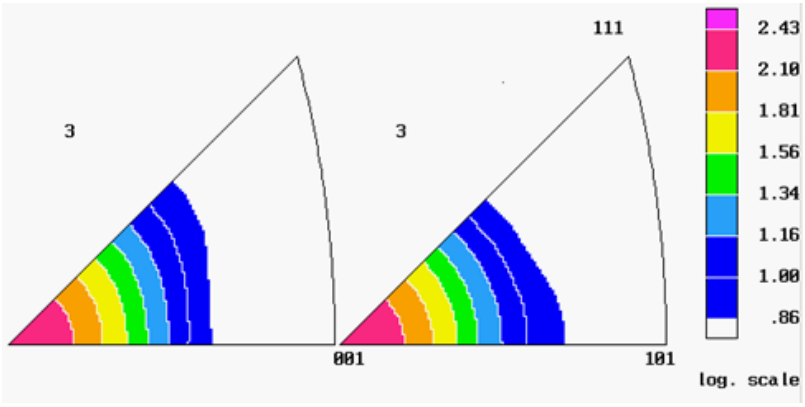

Figure 3. Inverse pole figure of the Heusler phase for axial direction before (left) and after (right) loading.

The neutron experiment with hydrostatic pressure was conducted using the instrument SEPD at IPNS, Argonne National Laboratories, USA. At ambient temperature, TOF spectra were collected for loading at 0, −176, −352 and −550 MPa, respectively.

The recorded TOF spectra were analysed using the GSAS software. In addition to the structure refinement, single peak fitting to a number of low index *hkl* planes was also performed on the Heusler phase to determine the individual diffraction peak properties such as the interplanar spacings and diffraction peak width. Lattice strains, ε_{hkl}, namely the strains in the normal of the lattice planes, can then be calculated from the measured interplanar spacings, d_{hkl}, according to the following equation:

$$\varepsilon_{hkl} = \frac{d_{hkl} - d_{0,hkl}}{d_{0,hkl}} \tag{1}$$

where $d_{0,hkl}$ is the stress-free reference interplanar spacing. In this paper, the strains were derived with respect to the initial state, which means zero strains in the powder before loading and in the bulk specimen at the initial holding stress (−5 MPa).

3. Results and discussion

3.1. Uniaxial compression

The initial texture in the cylindrical specimen was determined from the structure refinement of the neutron TOF spectra obtained at −5 MPa. The derived inverse pole figure (IPF) reveals a fibre texture with its $\langle 100\rangle_{\mathrm{HP}}$ grains lying in the specimen axis, as indicated by the left IPF in figure 3.

The macroscopic stress–strain curve recorded during the *in situ* uniaxial compression experiment (figure 2) shows three distinct stages, namely elastic loading up to −150 MPa, martensitic phase transformation between −150 and −350 MPa and reverse phase transformation during unloading. Beyond the elastic limit, a more rapid increase in strain marks the formation of the seven-layered martensite, which is revealed by the neutron TOF spectra presented later. At the peak compressive stress of this experiment, −350 MPa, the total accumulated strain reaches about −3.6%. It is interesting to notice that for the martensitic transformation stage deformation continued during the time when the applied load was kept constant to facilitate neutron diffraction measurement. This indicates that under the influence of the constant stress, martensitic transformation proceeded with time and the accumulated transformation strain at each load level gives the stress–strain curve a jerky appearance, as shown in figure 2. Upon unloading to −5 MPa, the strain was largely recovered by the reverse phase transformation, leaving a compressive strain of about −0.8% in the sample. Opposite to the forward transformation, continued reverse transformation results in a strain drop during holding at the unloading stress (figure 2). Young's modulus determined from the slope of the elastic curve in figure 2 is about 30 GPa.

Figure 4 plots the low Q range of the axial and transverse TOF spectra collected at several load levels. In the axial spectra (figure 4(a)), the seven-layered martensitic $(002)_{\mathrm{LP}}$ peak emerges at −150 MPa and grows at the expense of the Heusler $(200)_{\mathrm{HP}}$ peak that almost vanishes when the applied stress reaches −350 MPa. In the transverse spectra (figure 4(b)), the $(170)_{\mathrm{LP}}$ peak also grows with applied stress. Since the $(170)_{\mathrm{LP}}$ belongs to the $[001]_{\mathrm{LP}} \parallel$ LD grains, it can be inferred that the stress-induced transformation is characterized by a dominant structural change converting the $\langle 100\rangle_{\mathrm{HP}}$ fibre to the martensitic lattice correspondence variants (LCVs) with a mutual $[001]_{\mathrm{LP}}$ oriented in the loading direction. The formation of other LCVs is difficult to recognize on the figures. However, the absence of the $(170)_{\mathrm{LP}}$ peak in the axial spectrum and $(100)_{\mathrm{LP}}$ in the transverse spectrum at −350 MPa demonstrates that the $[001]_{\mathrm{LP}} \parallel$ TD LCVs cannot form under the uniaxial compression. Upon unloading, an almost fully reverse transformation occurred and the $\langle 100\rangle_{\mathrm{HP}}$ fibre texture is restored (figure 3). A much broader $(200)_{\mathrm{HP}}$ peak is obtained.

From the crystallographic correspondence between the parent and the transformed phase, lattice deformation associated with the martensitic transformation can be derived. Using the lattice parameters given before, the normal strains are calculated to be 0.025 for the $[1\bar{1}0]_{\mathrm{HP}}(\parallel [100]_{\mathrm{LP}})$, 0.017 for the $[110]_{\mathrm{HP}}(\parallel [010]_{\mathrm{LP}})$ and −0.047 for the $[001]_{\mathrm{HP}}(\parallel [001]_{\mathrm{LP}})$ crystallographic direction. This means that under uniaxial compression, the $[001]_{\mathrm{LP}} \parallel$ LD variants tend to develop first and in the $[100]_{\mathrm{HP}} \parallel$ LD grains, since such transformation

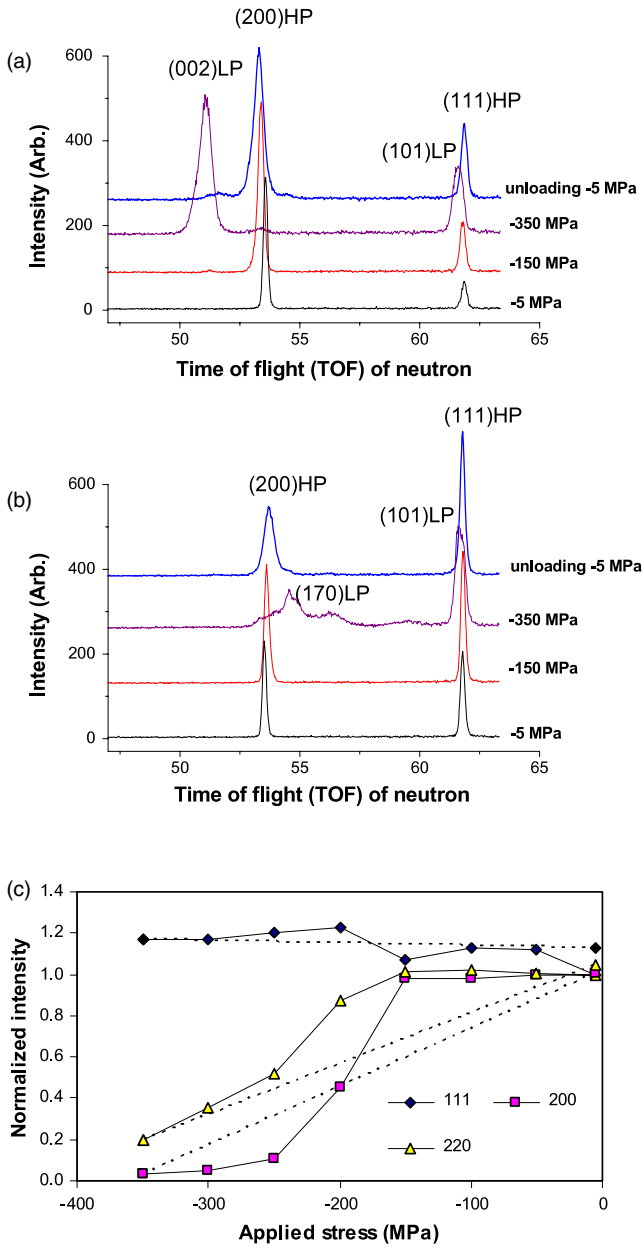

Figure 4. Diffraction profiles for the $(111)_{HP}$ and $(200)_{HP}$ along the loading direction (a) and transverse direction (b). The diffraction peak intensity changes for the HP phase are given in (c).

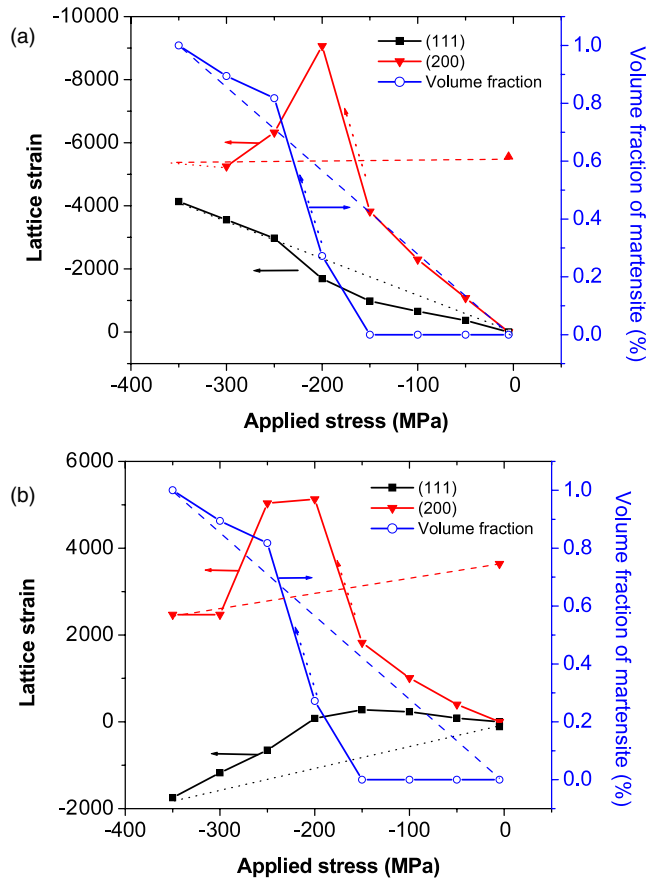

Figure 5. Axial (a) and transverse (b) lattice strain evolution under loading (solid lines) for the $(111)_{HP}$ and $(200)_{HP}$ orientations. Residual strains after unloading and the volume fraction of martensite are also shown.

yields the largest contraction in the compression axis and the $[100]_{HP}$ grains oriented in or near the loading direction have the largest Schemid's factor for their $(110)_{HP}[1\bar{1}0]_{HP}$ system on which transformation shear occurs. This is in accordance with the above observed diffraction peak intensity changes with applied stresses. Furthermore, it can be argued that since the formation of the $[001]_{LP} \parallel$ TD LCVs would lead to an axial elongation such structural changes are forbidden.

The lattice strain development with applied stress, which differs between the examined grain orientations as shown in figure 5, reveals clearly a microscopic, anisotropic behaviour of the Heusler phase during loading and unloading. None of the applied stress–lattice strain curves measured in the loading direction resembles the macroscopic behaviour shown in figure 2, indicating the influence of phase transformation strains as well as possible load partitioning between the Heusler and the martensitic phase. For the cubic Heusler phase, the $(111)_{HP}$ and $(200)_{HP}$ represent the two extremes in terms of elastic and plastic properties, therefore, further analysis will be continued on observations of the $(111)_{HP}$ and $(200)_{HP}$ peaks. The lattice strain evolution normal to these planes during loading (solid lines) and at unloading is illustrated in figure 5(a) for the loading direction (LD) and figure 5(b) for the transverse direction (TD). The initial linear strain development confirms the macroscopic observation of elastic limit at about −150 MPa. The compressive axial and tensile transverse strains develop in responding to the compressive axial stress, as expected for elastic loading. The elastic anisotropy of the Heusler phase is reflected by the different Young's modulus which is 156 GPa for the $(111)_{HP}$ and 38 GPa for the $(200)_{HP}$ planes, both of which are derived from the slope of the linear loading stage.

With the start of martensitic transformation at −150 MPa, the compressive axial $(200)_{HP}$ lattice strain increases more rapidly with applied stress. Further phase transformation beyond −200 MPa leads to a decreased axial strain which reaches −5000 microstrain at −300 MPa. Due to a too low peak intensity, the axial $(200)_{HP}$ cannot be determined for

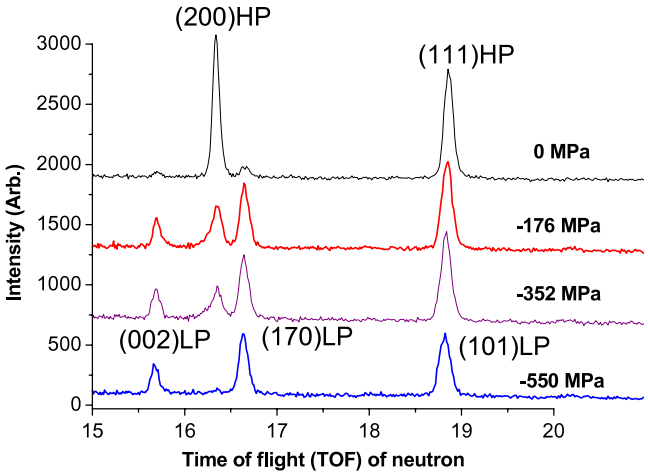

Figure 6. Diffraction profiles from hydrostatic pressure experiment.

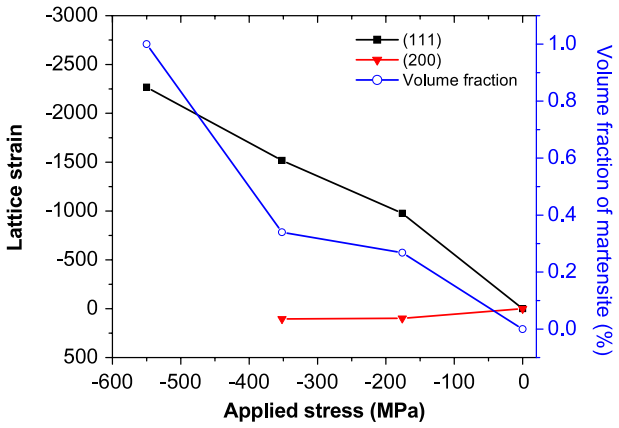

Figure 7. The $(111)_{HP}$ and $(200)_{HP}$ planes under hydrostatic pressure. The volume fraction of martensite is also shown.

−350 MPa. In the transverse direction, a similar change is observed for the tensile $(200)_{HP}$ strain showing a maximum at −200 MPa. Interestingly, Poisson's ratio for elastic loading is preserved to −200 MPa. The phase transformation imposes a different effect on the $(111)_{HP}$ grains. The compressive axial $(111)_{HP}$ strain increases monotonically, whereas an abnormal development of the transverse $(111)_{HP}$ strains towards a relatively large compression is observed. When the applied stress was removed, although the macroscopic strains largely relaxed, the $(200)_{HP}$ strain remains in both the loading and transverse directions. Accompanying this is also a retained peak broadening effect. On the other hand, no residual strain is found in either the axial or the transverse $(111)_{HP}$ planes. Evidently, the formation of the martensite phase causes large internal stresses in the parent phase, which are partially retained after the inverse transformation.

While the aforementioned transformation strains associated with the formation of the $[001]_{LP} \parallel$ LD grains contribute largely to the macroscopic strain, the interaction between the parent phase and the transformed phase leads to the development of the lattice strains observed between −150 and −200 MPa. Actually, Poisson's ratio indicates an elastic load transfer between the two phases. However, under further loading martensitic transformation in grains with less favourable orientation for transformation eventually becomes dominant. The diffraction peak intensity changes in figure 4(c) illustrates indeed that over −200 MPa transformation in the $[220]_{HP} \parallel$ LD grains is more important than that in the $[200]_{HP} \parallel$ LD grains. The influence of the phase transformation strain on the $(200)_{HP}$ becomes lower in both directions, which could be attributed to orientation of the new martensitic variants. The development of compressive $(111)_{HP}$ strains in both the loading and transverse directions can be associated with the phase transformation which induces a small contraction, about −0.0016, in all the $\{111\}_{HP}$ planes.

The macroscopic deformation that remains after unloading can be a reversible transformation strain (pseudoelasticity) that can be recovered after annealing or plastic deformation by slip. In either case, it is closely related to the behaviour of the $(200)_{HP}$, which retains a very large compressive strain in the LD and shows a very large diffraction peak width in both the LD and TD directions.

3.2. Hydrostatic compression

The seven-layered martensite also forms under the application of hydrostatic pressure (figure 6), however with different characteristics from the uniaxial stress-induced transformation. Apparently, the formation of martensite is much more difficult. At −352 MPa, only 35% transformation product is obtained, in comparison with the almost fully transformation at −350 MPa in the uniaxial loading. It is only after reaching −550 MPa that the phase transformation is complete. Furthermore, the isotropic compression facilitates the formation of the $[001]_{LP} \parallel$ LD in all sample directions. As a result, both $(002)_{LP}$ and $(170)_{LP}$ peaks appear in figure 6.

Anisotropic lattice strains are also found to develop with increasing pressure (figure 7), which is, however, much smaller in comparison with the uniaxial loading. While the elastically stiff $(111)_{HP}$ lattice planes accumulates compressive strains, the elastically soft $(200)_{HP}$ lattice planes show almost no strains. On the other hand, peak broadening is obvious for the former but very little for the latter. Due to the large load increment, it is not clear whether there exists an elastic loading stage. Elastic strains induced by any hydrostatic stresses are related to Young's modulus E_{hkl} and Poisson's ratio ν_{hkl} through the following equation:

$$\varepsilon_{hkl} = \frac{\sigma}{E_{hkl}}(1 - 2\upsilon_{hkl}). \tag{2}$$

Poisson's ratio derived from the *in situ* compression experiment is approximately 0.5 for the $(200)_{HP}$, which means that the elastic contribution of the hydrostatic load to the lattice strains is essentially zero. With Poisson's ratio of 0.35 and Young's modulus of 156 GPa, the elastic strain under the peak stress, −550 MPa, is estimated to be 1000 microstrain for the $(111)_{HP}$. Apparently, while the phase transformation imposes no lattice strains on the $(200)_{HP}$, it induces an additional compressive strain on the $(111)_{HP}$, which reaches −1500 microstrain at the peak stress. The correlation of the lattice

strain development can again be inferred by examining the transformation strains. As shown in the previous section, the formation of the $[001]_{LP}$ variants is accompanied by a contraction of 0.047 in the $[001]_{HP}$. Moreover, it can be derived that elongation in the $[100]_{HP}$ and $[010]_{HP}$ is 0.021, almost half of the $[001]_{HP}$ strain. Therefore, it can be reasonably assumed that interactions between different orientated $[001]_{LP}$ LCVs can cancel the $(200)_{HP}$ strains and leave a very small lattice strain. The deformation in the $\{111\}_{HP}$, which is independent of the orientation of the plane, contributes to the net compressive strain observed.

4. Conclusions

In situ neutron experiments were carried out on a $Ni_{48}Mn_{30}Ga_{22}$ alloy under uniaxial and hydrostatic compression, respectively. Large lattice strains develop with transformation plasticity during uniaxial loading and their anisotropic behaviour indicates the generation of intergranular stresses. In spite that the transformations HP $\Rightarrow$ LP $\Rightarrow$ HP are essentially reversible in terms of crystallographic texture, the lattice strains and peak broadening effect develop during the HP $\Rightarrow$ LP transformation remain with certain crystallographic planes after the reverse transformation. While the $(200)_{HP}$ planes retain a large residual lattice strain and a broader peak, the $(111)_{HP}$ planes show a pseudoelastic behaviour with both the strain and the peak width being restored after the LP $\Rightarrow$ HP transformation.

Anisotropic strains represented by essentially zero $(200)_{HP}$ strains and compressive $(111)_{HP}$ strain development are observed in the hydrostatic experiment. The formation of martensite is also found more difficult, which could be explained by the low internal stresses associated with the transformation. The $(200)_{HP}$ planes, which remain almost stress-free through the whole phase transformation process, could play an important role in the martensitic transformation.

Acknowledgments

The authors are grateful to the National Natural Science Foundation of China (Grant No. 50531020) and the Swedish Research Council in the framework of the SIDA project (Grant No. 348-2004-3475) for their financial support. This research project has also been supported by the European Commission under the 6th Framework Programme through the Key Action: Strengthening the European Research Area, Research Infrastructures (Contract no. HII3-CT-2003-505) and the 111 Project (B07015) of the Ministry of Education of China and the National Science Foundation International Materials Institutes (IMI) Program (DMR-0231320), with Dr C Huber as the Program Director.

References

[1] Ullakko K, Huang J K, Kantner C, O'Handley R C and Kokorin V V 1996 *Appl. Phys. Lett.* **69** 1966
[2] Söderberg O, Ge Y, Sozinov A, Hannula S-P and Lindroos V K 2005 *Smart Mater. Struct.* **14** S223
[3] Chernenko V A, Kokorin V V, Babii O M and Zasimchuk I K 1998 *Intermetallics* **6** 29
[4] Pons J, Chernenko V A, Santamarta R and Cesari E 2000 *Acta Mater.* **48** 3027
[5] Brown P J, Crangle J, Kanomata T, Matsumoto M, Neumann K-U, Ouladdiaf B and Ziebeck K R A 2002 *J. Phys.: Condens. Matter* **14** 10159
[6] Martynov V V and Kokorin V V 1992 *J. Physique* III **2** 739
[7] Wang W H, Liu Z H, Zhang J, Chen J L, Wu G H and Zhan W S 2002 *Phys. Rev.* B **66** 052411
[8] Huang X, Ackland G J and Rabe K M 2003 *Nat. Mater.* **2** 307
[9] Wang Y-D *et al* 2006 *Adv. Mater.* **18** 2392–6
[10] Cong D Y, Wang Y D, Zetterström P, Peng R L, Delaplane R, Zhao X and Zuo L 2005 *Mater. Sci. Tech.* **21** 1412